Bipolar magnetic semiconductors emerging in graphene nanoribbons with zigzag edges and internal defects

Yangkai Cheng,[1,*] Jing Xu,[1,*] Jiang Xiang,[1] Wei Liu,[1,†] and Maosheng Miao[2]

[1]*Department of Optical Engineering, College of Optical, Mechanical and Electrical Engineering, Zhejiang A & F University, Hangzhou, Zhejiang 311300, People's Republic of China*

[2]*Department of Chemistry & Biochemistry, California State University, Northridge, California 91330-8262, USA*

(Received 25 April 2024; revised 2 July 2024; accepted 9 August 2024; published 21 August 2024)

Bipolar magnetic semiconductors (BMSs) enable controlled spin polarization for advanced spintronic applications. However, their applications are greatly hindered by the limited number of available BMS materials. We demonstrate a family of egg-tray graphene nanoribbons (EGNRs) featuring both zigzag edges and internal defects (pentagons and heptagons) constructed by slicing egg-tray graphene. First-principles calculations show that these EGNRs exhibit distinguished BMS behavior, along with other spintronic properties such as half-metallicity and spin-gapless semiconductivity (SGS). Most notably, when the width of EGNRs is small, the internal defect regions significantly influence the spin density distribution of the entire ribbon, resulting in spin polarization not only localized at the edge carbon atoms but also across the defect areas. The synergistic effect between these distinct regions promotes the formation of stable BMSs. The calculations also show a gradual transition from BMS to semiconductor or half-metal, controlled by the edge states while the width of EGNRs increases. Furthermore, including pentagons and heptagons at the edges of EGNRs compresses BMS behavior, transforming the material into an SGS. In this paper, we provide a route to achieve and control BMSs in a family of carbon nanoribbon materials based on the combination of edge cutting and topology control of graphene materials.

DOI: 10.1103/PhysRevB.110.085141

I. INTRODUCTION

Spintronics, which leverages both the spin and charge of electrons, has the advantages of high data storage density, high energy efficiency, and fast information processing speeds, holding significant potential in the fields of magnetic memory, quantum computing, and sensors [1,2]. Bipolar magnetic semiconductors (BMSs) are cutting-edge functional spintronic materials characterized by opposing spin-polarization directions at the valence band maximum (VBM) and conduction band minimum (CBM) [3–6]. Utilizing BMSs enables the achievement of complete spin polarization of the current, with the polarization direction modifiable via gate voltage application. The unique electronic properties of BMSs, such as controllability of spin direction [7,8] and giant magnetoresistance effect [9,10], reveal their substantial potential in spintronic applications, including spin filters, spin valve functionality, magnetic storage devices, and sensors [4,5,11–14]. However, the unique spin properties of BMSs pose some challenges to their design, which have limited the diversity of known BMSs and consequently hindered further exploration of BMS applications [6,15–17]. Therefore, seeking effective strategies to discover various types of BMSs is both highly valuable and urgently needed [18,19].

Two-dimensional (2D) graphene-derived materials are considered promising candidates for spintronic materials due to their ultrahigh carrier mobility and unique electronic and magnetic properties [20–23]. However, the lack of intrinsic magnetism in pristine graphene greatly restricts its applications in spintronic devices. Cutting graphene along specific orientations yields zigzag graphene nanoribbons (ZGNRs), which exhibit edge-dependent magnetism and adjustable electronic features [24–27]. Authors of recent studies have revealed that the electronic and magnetic properties of ZGNRs can be effectively modulated through various methods, such as applying in-plane electric fields, incorporating defects, and altering edge chemistries [28–31]. For instance, ZGNRs could achieve half-metallicity by applying external in-plane uniform electric fields [28]. This effect can also be induced by chemically modifying the edges of ZGNRs with different functional groups, like NO_2 and CH_3, offering a method to adjust their magnetic characteristics [29]. Additionally, ZGNRs can be transformed into BMSs by introducing nanopores or by asymmetrically decorating the two edges with hydrogen [30]. Despite these strategies, however, up to now, pure carbon-based materials identified as BMSs remain extremely rare. Motivated by these noteworthy findings, we aim to investigate a strategy for manipulating the electronic and magnetic properties of graphene nanoribbons by harnessing the synergistic effects of edge and internal defects, ultimately aiming to achieve carbon-based BMSs and uncovering other intriguing spintronic properties.

Egg-tray graphene (ETG), a class of 2D graphene allotropes we previously proposed, are constructed through the

*These authors contributed equally to this work.
†Contact author: weiliu@zafu.edu.cn

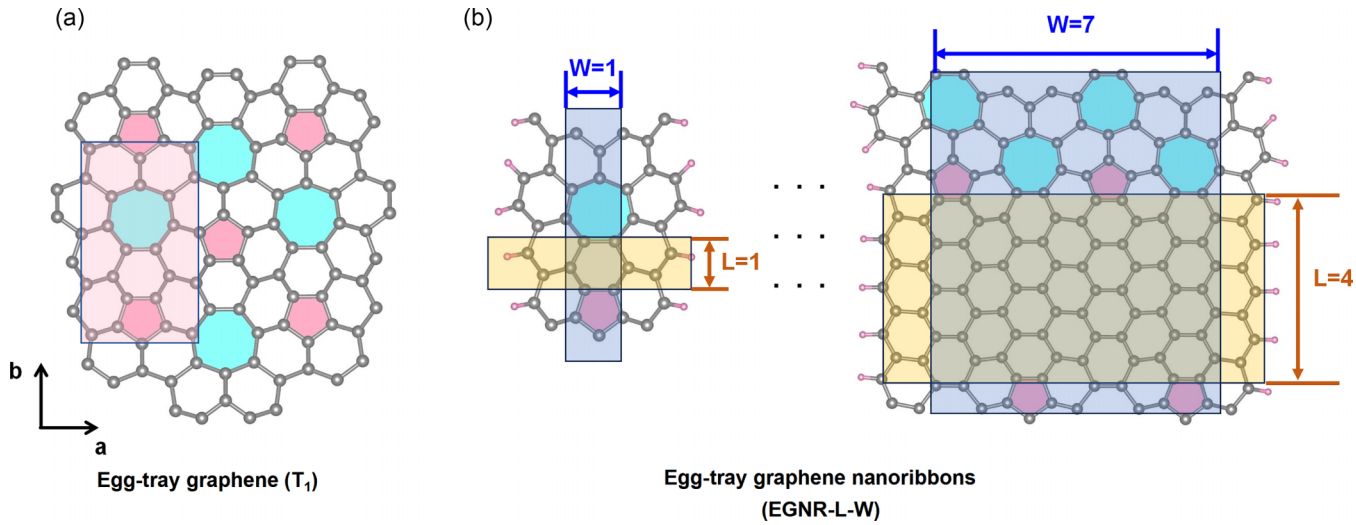

FIG. 1. Top views of (a) egg-tray graphene (T_1) and (b) egg-tray graphene nanoribbons (EGNRs) EGNR-*L*-*W* (EGNR-1-1 and EGNR-4-7). *L* denotes the number of hexagonal rings located between the heptagonal and pentagonal rings, *W* refers to the width of the nanoribbons, excluding the edges.

topological arrangement of pentagons and heptagons within the graphene lattice [32]. By selectively slicing specific ETG, graphene nanoribbons characterized by both zigzaglike edges and internal defects can be generated. In this paper, we employed first-principles calculations to explore the stability, magnetism, and electronic properties of these derived nanoribbons, aiming to understand how the synergistic effects of edges and internal defects influence their electronic and magnetic characteristics. The results demonstrate that these nanoribbons exhibit excellent thermodynamic and kinetic stability, with the edge-defect synergy facilitating robust BMS formation. Additionally, in this paper, we highlight how quantum confinement, edge configurations, and defect-induced states markedly influence BMS characteristics. Other valuable spintronic properties can also be generated, such as half-metallicity and spin-gapless semiconductor (SGS) behaviors, highlighting the potential of ETG-derived nanoribbons in advanced spintronic applications.

II. CALCULATION METHOD

In this paper, first-principles calculations based on density functional theory [33] were conducted using VASP [34]. The ion-electron interaction was described using the projector augmented-wave method [35]. The Perdew-Burke-Ernzerhof functional [36] with spin-polarized gradient corrections and the screened Heyd-Scuseria-Ernzerhof (HSE06) functional [37] were used to describe the exchange and correlation interactions. The energy cutoff was set to 550 eV. The convergence threshold for the total energy per atom was set to 10^{-5} eV, and the atomic forces were optimized to be <0.01 eV/Å. A vacuum layer of 15–20 Å was introduced along the *Z* and *X* directions to avoid interactions between adjacent layers. For the sampling of the first Brillouin zone, 1 × 2 × 1, 1 × 15 × 1, and 1 × 30 × 1 k-point grids were employed for structure optimization, self-consistency calculations, and electronic properties calculations, respectively [38].

III. RESULTS AND DISCUSSION

ETG is a series of single-layer, 2D crystalline structures constructed by periodically replacing some hexagons in graphene sheets with pentagons and heptagons in specific topological orders. This topological arrangement endows ETG with a diverse range of electronic properties, from semimetallic to semiconducting with a tunable band gap. Additionally, it exhibits superior mechanical properties, such as a negative Poisson's ratio [32]. Figure 1(a) displays the structure of ETG T_1, which has the smallest unit cell among all types of ETG. The defective rings (pentagons and heptagons) are separated by hexagonal rings, forming a robust topological structure. Liu *et al.* [32] have affirmed the dynamic stability of these graphene allotropes using first-principles calculations. By slicing ETG T_1 along the *b* direction, as shown in Fig. 1(a), one-dimensional (1D) ETG nanoribbons (EGNRs) are created, which are named as EGNR-*L*-*W*. Here, *L* denotes the number of hexagonal rings located between the heptagonal and pentagonal rings, as highlighted in yellow in Fig. 1(b) ($L = 1, 2, 3$, etc.), and *W* refers to the width of the nanoribbons, excluding the edges, and is quantified by the number of hexagon chains ($W = 1, 3, 5$, etc.). In these EGNRs, the edges consist of hexagons only, while the pentagons and heptagons are situated at the center of the nanoribbons. Figure 1(b) shows the structures of two typical EGNRs: EGNR-1-1 and EGNR-4-7. All carbon atoms in EGNRs are sp^2 hybridized, with each heptagonal ring surrounded by seven hexagonal rings and each pentagonal ring surrounded by five hexagonal rings. In this paper, the carbon atoms located at the edges of these nanoribbons are passivated with hydrogen. The widths of all the EGNRs are listed in Table S1 in the Supplemental Material [39].

The structural stability of EGNRs was shown by the binding energies calculated as the following:

$$E_B = \frac{E_{\mathrm{EGNR}} - n_H \times E_H - n_C \times E_C}{n_H + n_c}, \tag{1}$$

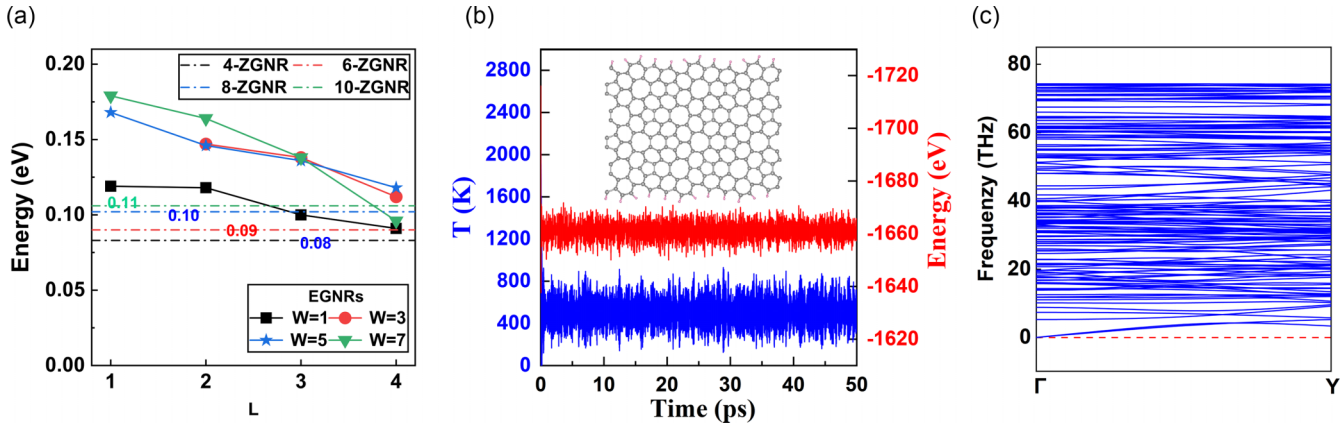

FIG. 2. (a) Binding energies of egg-tray graphene nanoribbons (EGNRs) as a function of L and W. Black squares, red circles, blue five-pointed stars, and green triangles represent EGNR-L-1, EGNR-L-3, EGNR-L-5, and EGNR-L-7 (L = 1, 2, 3, and 4), respectively. Dashed lines indicate the binding energies of n-ZGNR (n = 4, 6, 8, and 10). (b) Variations in simulated energy and temperature during the *ab initio* molecular dynamics (AIMD) simulations of EGNR-1-7 over 50 ps with a time step of 1 fs. (c) Phonon spectra of EGNR-1-7.

where E_B, E_{EGNR}, E_H, and E_C represent the binding energy, the total energy of EGNRs, and the energies of the H and C atoms obtained from the H_2 molecule and graphene, respectively. Here, n_H and n_C represent the total number of H and C atoms. As shown in Fig. 2(a), the binding energies of EGNRs exhibit a dependence on their dimensions, increasing with W but decreasing with L. This observation suggests that broader nanoribbons tend to destabilize the EGNRs, whereas a greater separation between the pentagonal and heptagonal rings enhances their stability. Therefore, EGNR-1-7 exhibits the highest binding energy of 0.18 eV. Notably, as W increases, the binding energies of EGNRs progressively converge toward that of ETG T_1, which is 0.24 eV. Nonetheless, the binding energies of EGNR-L-W (L = 1, 2, 3, and 4; W = 1, 3, 5, and 7) fall within a narrow range of 0.18–0.09 eV. The binding energies of ordinary ZGNRs with similar widths (n-ZGNRs, n = 4, 6, 8, and 10) range from 0.11 to 0.08 eV, as shown in Fig. 2(a). For structures of similar width, EGNRs exhibit slightly higher energies of 0.006–0.073 eV per atom than ZGNRs. Moreover, as L increases, the binding energies of EGNRs converge toward those of ZGNRs. For instance, at L = 4, the binding energies of EGNRs exceed those of ZGNRs of the same width by only 0.006–0.012 eV per atom. The binding energies of EGNRs are also comparable with the binding energies of the recently reported penta-hexa-graphene-nanoribbons (PHGNRs) [40], situated in the 0.20–0.11 eV range. This comparability, along with the proven stability of ZGNRs and PHGNRs, implies a similar stability for EGNRs.

Subsequently, the thermal and dynamic stabilities of EGNR-1-7, which has the highest binding energy, are further examined through *ab initio* molecular dynamics (AIMD) simulations and phonon spectra analysis. The AIMD simulation was conducted on a 1 × 4 supercell of EGNR-1-7 over 50 000 steps (50 ps) at 500 K [41,42]. The results depicted in Fig. 2(b) show that EGNR-1-7 can maintain its topological structure, with the energy oscillating near the equilibrium state throughout the simulation process, indicating its good thermal stability. The phonon spectrum of EGNR-1-7, displayed in Fig. 2(c), shows no imaginary frequencies in the examined Brillouin zone. This absence of imaginary frequencies implies stability at the equilibrium positions within the crystal structure. The resonant frequency distribution, representing atomic vibrations near their equilibrium positions, exhibits no signs of instability or instances where characteristic frequencies assume negative values, which confirms that EGNR-1-7 is dynamically stable. Currently, narrow ZGNRs are usually synthesized using bottom-up chemical methods [43,44]. In recent years, remarkable advancements have been made in the bottom-up chemical synthesis of nanographenes and low-dimensional carbon-based materials, highlighting the creation of complex structures with nonhexagonal carbon rings (like pentagons and heptagons) to form unique geometries [45–49]. This greatly enhances the experimental feasibility of EGNRs. Notably, a saddle-shaped polycyclic aromatic hydrocarbon featuring two heptagonal and two pentagonal rings was successfully synthesized [45]. This molecule can be viewed as a segment of graphene nanoribbon derived from cutting ETG. Therefore, it may serve as a segment or synthetic precursor for EGNRs. Other graphene nanoribbons based on ETG also show promise for synthesis using similar methods. Collectively, these findings suggest that these EGNRs have good thermodynamic stability and significant potential for fabrication via bottom-up chemical synthesis methods.

To show the magnetic ground state of EGNRs, their energies were calculated under different spin states: ferromagnetic (FM), antiferromagnetic (AFM), and nonmagnetic (NM). As illustrated in Fig. 3, when the value of W is 1, only EGNR-1-1 exhibits a NM state, while all other EGNRs are in the AFM state. With increasing W, all EGNR-L-W's transition to a FM ground state. These shifts of magnetism in ground state, influenced by variations in W, are attributed to the intrinsic strain within the nanoribbons. Previous researchers have demonstrated that the magnetic ground state of penta-hexa-graphene can undergo a transition from AFM to FM under the influence of specific uniform biaxial tensile or compressive strains [40,50]. In the case of EGNRs, when ETG is cut into nanoribbons, inherent bending stress occurs due to the curved structure. The degree of curvature gradually increases with the increase of W, leading to a corresponding increase in

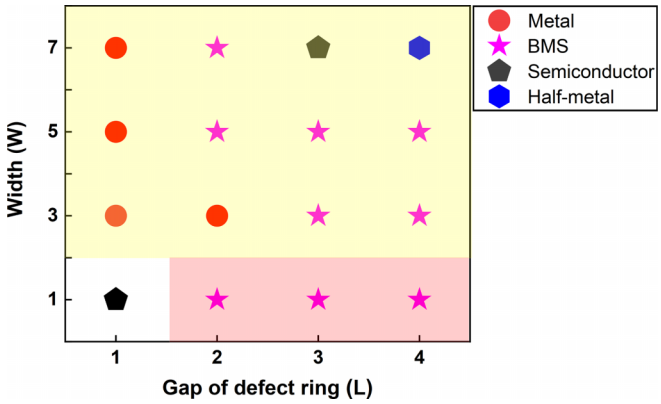

FIG. 3. Magnetic and electronic properties of egg-tray graphene nanoribbons (EGNRs) as a function of L and W. Nonmagnetic (NM), antiferromagnetic (AFM), and ferromagnetic (FM) ground states are indicated by white, red, and yellow background, respectively. Red circles, purple five-pointed stars, black pentagons, and blue hexagons represent metal, bipolar magnetic semiconductor (BMS), semiconductor, and half-metal.

compressive strain. Once the compressive strain surpasses a critical value, the transformation from AFM to FM is realized. The thermal stability of these EGNRs was also investigated by calculating the total energy difference ($\Delta E = E_{\mathrm{AFM}} - E_{\mathrm{FM}}$), with results ranging from 41 to 71 meV. These results suggest that EGNRs possess a sufficiently high-energy difference to maintain their magnetic state against thermal fluctuations.

The Curie temperatures (T_c) of EGNRs with BMS characteristics were also predicted using the Monte Carlo method as implemented in the software package developed by Zhang *et al.* [51]. The results indicate that EGNR-2-7 has the highest Curie temperature of 95 K. The magnetic moment (M) and magnetic susceptibility (χ) of EGNR-2-7 is plotted in Fig. S1 in the Supplemental Material [39]. While this T_c is ∼10 times higher than that of ZGNRs (<10 K) [52,53] and much higher than partially hydrogenated graphene nanoribbons (∼3.4 K) [54], it is still much lower than room temperature.

Authors of previous studies have shown that carrier doping (electrons and holes) can transform the magnetic ground state of ZGNRs from AFM to FM [55,56]. In this context, EGNR-2-1 serves as an example to investigate the effect of carriers doping on the magnetic ground states of EGNRs. Figure S2 in the Supplemental Material [39] shows the total energy difference ($\Delta E = E_{\mathrm{AFM}} - E_{\mathrm{FM}}$) per unit cell as a function of electron and hole concentration. As observed, when EGNR-2-1 is doped with carriers (either electrons or holes), the energy difference gradually increases with increasing doping concentration. Notably, when the doping level reaches 0.5 carriers per unit cell, the energy difference becomes positive, indicating a transition in the ground state of EGNR-2-1 from AFM to FM.

The electronic properties of EGNRs were analyzed through their band structures, as shown in Fig. 4. EGNR-1-1 is identified as a NM semiconductor, displaying completely degenerate spin-up and spin-down bands, with a band gap measured at 0.37 eV, as shown in Fig. 4(a). We investigate the effect of dimensional parameters on electronic characteristics, by varying L or W, respectively. As shown in Figs. 4(b), 4(e), and 4(f), an increasing nondegeneracy is observed as the dimension L changes from 1 to 4. The resulting band structures of EGNR-L-1 (where L = 2, 3, and 4) indicate that all the

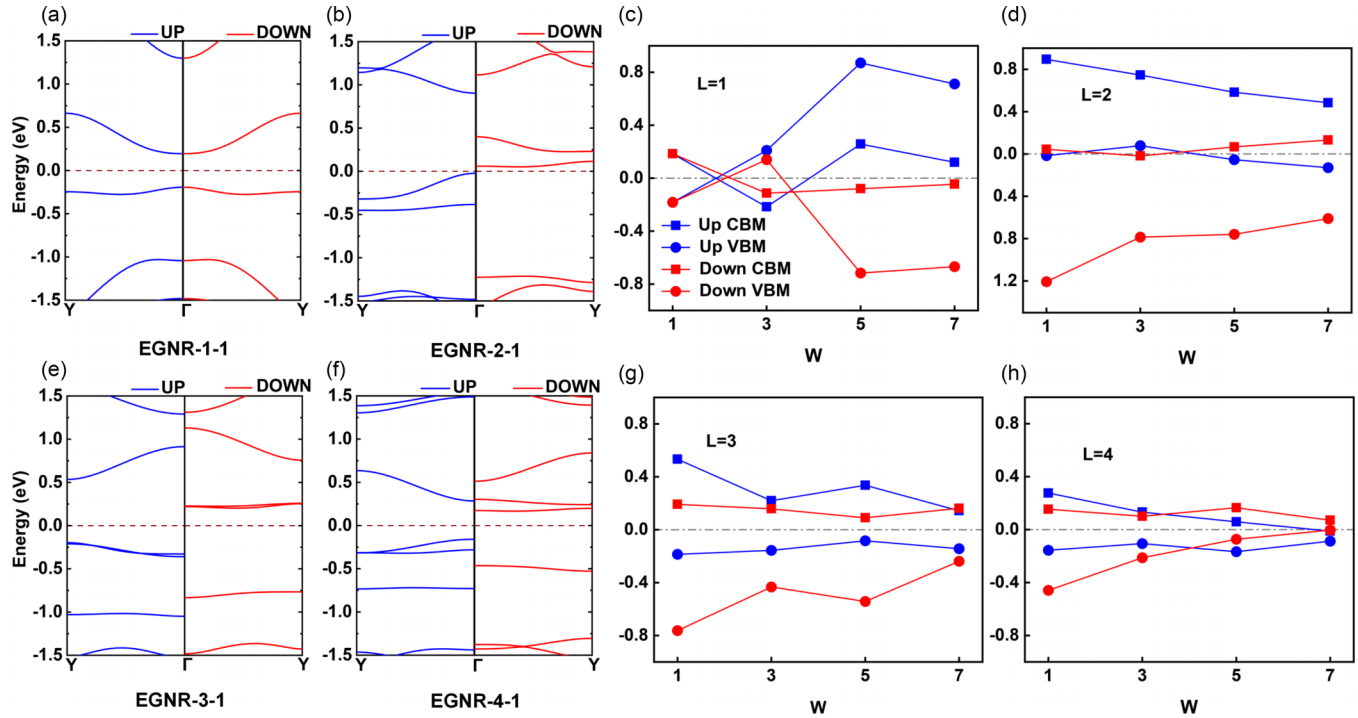

FIG. 4. Band structures of egg-tray graphene nanoribbons (EGNRs): (a) EGNR-1-1, (b) EGNR-2-1, (e) EGNR-3-1, and (f) EGNR-4-1. Variations of conduction band minimum (CBM) and valence band maximum (VBM) with respect to W for (c) EGNR-1-W, (d) EGNR-2-W, (g) EGNR-3-W, and (h) EGNR-4-W (W = 1, 3, 5, and 7), respectively. Blue represents spin up channel, red represents spin down channel. Square represents CBM, circle represents VBM.

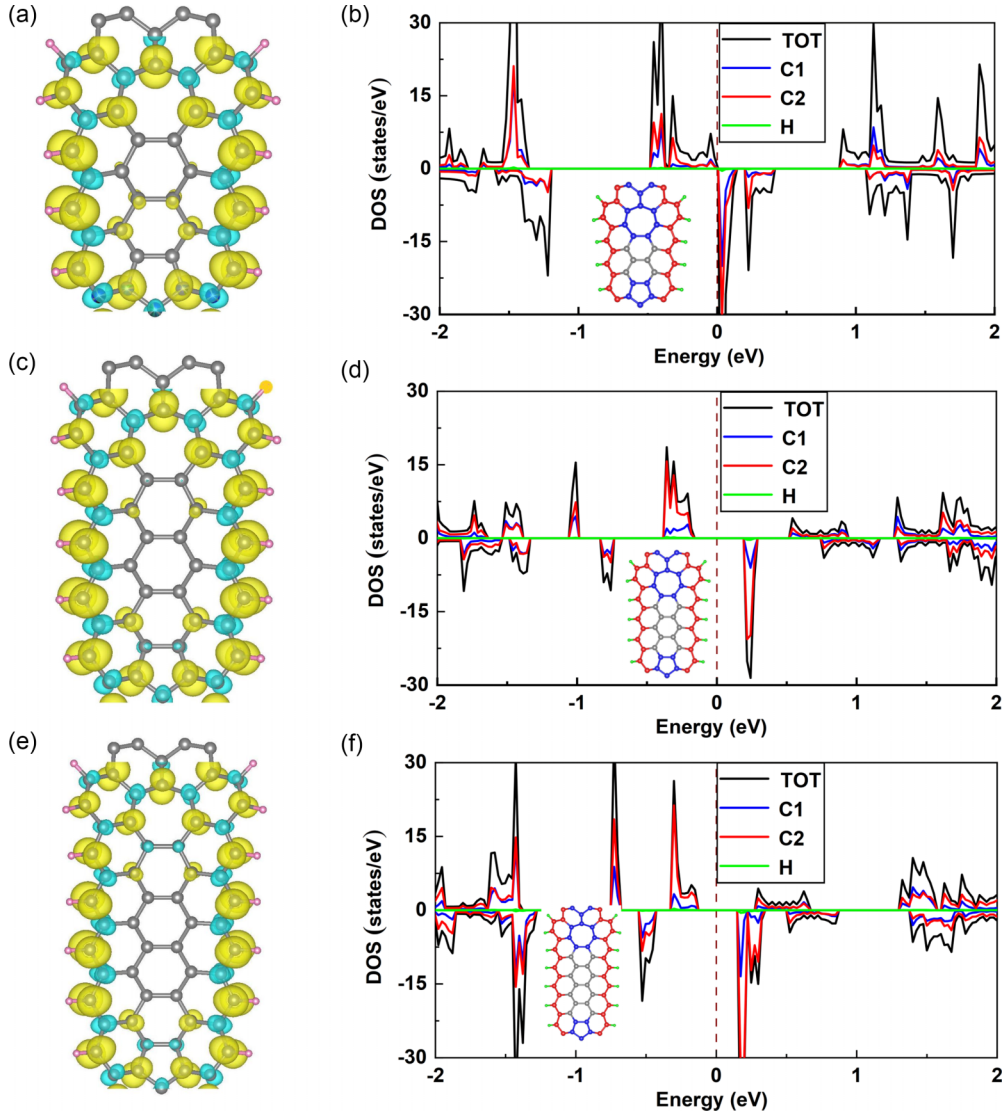

FIG. 5. Spin density distributions and projected density of states for egg-tray graphene nanoribbons (EGNRs): (a) and (b) EGNR-2-1, (c) and (d) EGNR-3-1, and (e) and (f) EGNR-4-1. The value of the isosurface level is 0.002 e/Å^3. Black represents the total density of states (DOS); blue, red, and green represent the projected DOSs (PDOSs) of the internal defect carbon atoms (C1), edge carbon atoms (C2), and hydrogen atoms (H), respectively.

CBM states are in the spin-down channel, while all the VBM states are in the spin-up channel, demonstrating typical BMS characteristics.

To explore the influence of W on the electronic and magnetic properties of EGNRs, we fixed L at values of 1, 2, 3, and 4 and then examined the effects of incrementally increasing W from 1 to 3, 5, and 7. The corresponding structures and band structures are depicted in Figs. S3 and S4 in the Supplemental Material [39]. As shown in Figs. 4(c), 4(d), 4(g), and 4(h), EGNR-1-1 is a NM semiconductor with overlapping VBM and CBM in both spin channels, characterized by high degeneracy. However, this degeneracy diminishes with increasing W. For instance, in Figs. 4(c) and S4 in the Supplemental Material [39] with $L = 1$, the band structures of EGNR-1-W ($W = 3$, 5, and 7) reveal intersections and crossings of both spin-up and spin-down bands at the Fermi level, classifying these three EGNRs as magnetic metals. In the scenario of $L = 2$, as shown in Figs. 4(d) and S4 in the Supplemental Material [39], only EGNR-2-3 exhibits magnetic metal characteristics. The remaining structures, with CBMs in the spin-down channel and VBMs in the spin-up channel, demonstrate BMS characteristics. As L increases to 3, as depicted in Figs. 4(g) and S4 in the Supplemental Material [39], EGNR-3-1, EGNR-3-3, and EGNR-3-5 all display BMS characteristics. However, with a further increase in W, the CBM in the spin-down channel of EGNR-3-W is observed to be higher than its counterpart in the spin-up channel, suggesting that EGNR-3-7 has its CBM and VBM exclusively in the spin-up channel, indicative of magnetic semiconductor properties. Moreover, when W is extended further such that EGNR-3-W transforms into a 2D plane, as shown in Figs. S5(a) and S5(b) in the Supplemental Material [39], its band structure reveals NM Dirac semimetal properties. Lastly, as shown in Figs. 4(h) and S4 in the Supplemental Material [39], EGNR-4-1, EGNR-4-3, and EGNR-4-5 also exhibit characteristics of BMSs. However, EGNR-4-7 demon-

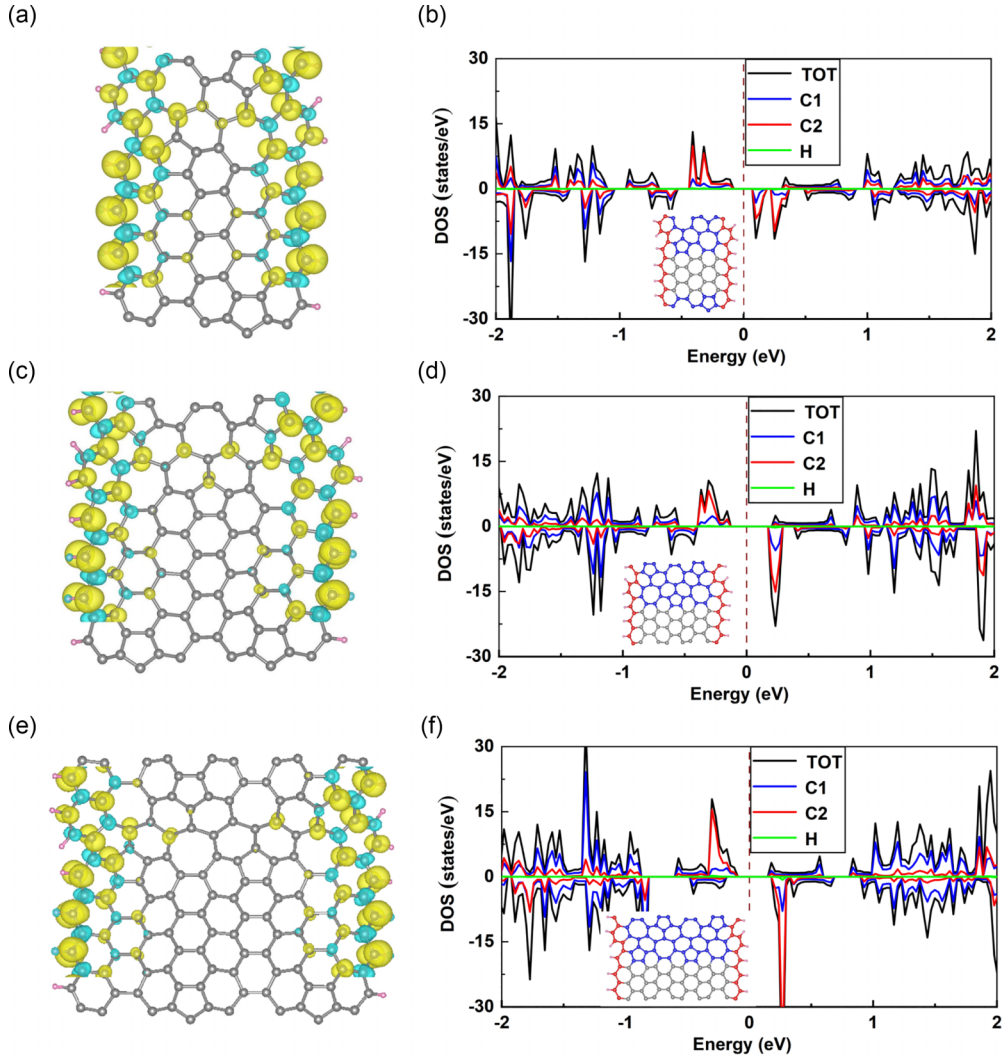

FIG. 6. Spin density distributions and projected density of states for egg-tray graphene nanoribbons (EGNRs): (a) and (b) EGNR-3-3 and (c) and (d) EGNR-3-5, and (e) and (f) EGNR-3-7. The value of the isosurface level is 0.002 e/Å^3. Black represents the total density of states (DOS); blue, red, and green represent the projected DOSs (PDOSs) of the internal defect carbon atoms (C1), edge carbon atoms (C2), and hydrogen atoms (H), respectively.

strates distinct electronic properties in its two spin channels. In the spin-up channel, the CBM falls below zero, indicating that the band crosses the Fermi level and exhibits metallic characteristics. Conversely, in the spin-down channel, EGNR-4-7 presents a small band gap of 0.09 eV, signifying semiconductor properties. This combination of metallic behavior in one spin channel and semiconducting behavior in the other classifies EGNR-4-7 as a spin-semimetal. When W is extended further such that EGNR-4-W transforms into a 2D plane, as shown in Figs. S5(c) and S5(d) in the Supplemental Material [39], its band structure demonstrates NM semiconductor properties. These findings reveal that the BMS behavior in EGNRs primarily exists in narrow 1D structures and is highly dependent on the size of W. Once a specific threshold is exceeded, the BMS characteristics disappear.

The summarized results of the magnetic and electronic properties of EGNRs are presented in Fig. 3, showing that no EGNRs with the smallest L value of 1 do exhibit BMS properties and that BMSs disappear when W is large. To investigate the origin of BMSs, we plot spin densities and projected densities of states (PDOSs) [57] for EGNR-2-1, EGNR-3-1, and EGNR-4-1, which all exhibit BMS properties. The obtained results are depicted in Fig. 5, which shows that the spin density is predominantly localized in the defect areas at the center and edge regions. Notably, the spin density distribution at the edge regions is more pronounced than that in the central defect regions. Additionally, the spin density between adjacent atoms varies in direction, implying the presence of negative exchange interaction between the nearest-neighboring atoms. Authors of previous reports have highlighted that magnetism primarily concentrates at the edges in magnetic ZGNRs [58,59]. As shown in Fig. S6 in the Supplemental Material [39], the spin distribution of 4-ZGNRs, which have a width like that of EGNR-L-1 ($L = 2$, 3, and 4), mainly resides on the carbon atoms at the edge, with only minimal spin observed on some carbon atoms near the edge. The presence of internal defect regions (pentagons and heptagons) significantly influences the spin density distribu-

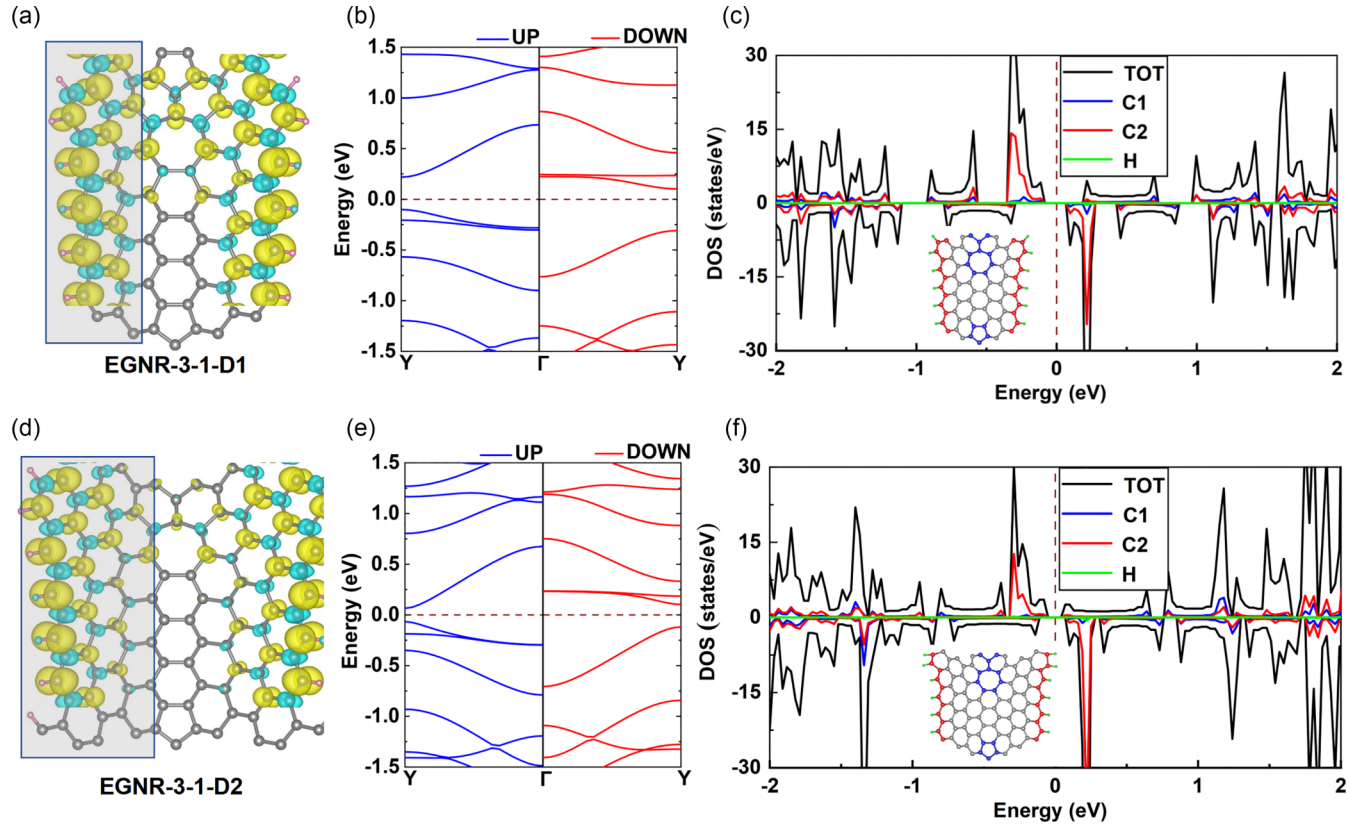

FIG. 7. Spin density distributions, band structures, and projected densities of states (PDOSs) for egg-tray graphene nanoribbons (EGNRs): (a)–(c) EGNR-3-1-D1 and (d)–(f) EGNR-3-1-D2. The value of the isosurface level is 0.002 e/Å^3. Black represents the total density of states (DOS); blue, red, and green represent the PDOSs of the internal defect carbon atoms (C1), edge carbon atoms (C2), and hydrogen atoms (H), respectively.

tion throughout the entire ribbon, resulting in spin polarization across the defect areas. Next, we analyzed the PDOSs of the internal defect carbon atoms (C1), the edge carbon atoms (C2), and the hydrogen atoms (H), as shown in Figs. 5(b), 5(d), and 5(f), respectively. It is evident that the peaks near the Fermi level in the total DOS are mainly contributed by the internal defect and edge carbon atoms, with the contribution from H atoms being almost negligible. Additionally, the contribution from the edge carbon atoms is more substantial. Therefore, we speculate that the BMSs in EGNRs originate from the interactions between localized magnetic moments, which arise from unpaired electrons localized at both the edge and internal defect carbon atoms.

The spin density distributions and PDOSs for EGNR-3-3, EGNR-3-5, and EGNR-3-7 are depicted in Fig. 6. It is observed that EGNR-3-1 [see Fig. 5(c)] showcases noticeable spin density within the central defect regions constituted by heptagonal and pentagonal carbon rings. However, as W increases, the spin density distribution on the internal defect carbon atoms gradually diminishes. In EGNR-3-7, the spin density is notably absent in the central defect regions, being confined solely to the hexagonal edge carbon atoms and their immediate neighbors. This observation suggests that, in narrower ribbons, the defect regions (pentagons and heptagons) significantly influence the electronic structure of the entire ribbon, leading to spin polarization throughout the defect areas. As W increases, the influence of the central defects on the overall electronic structure diminishes. In very wide nanoribbons, such as EGNR-3-7, the central defects become too distant from the edges to affect the edge states significantly. Therefore, the spin density is observed mainly at the edges and adjacent carbon atoms. According to PDOS analysis [see Figs. 6(b), 6(d), and 6(f)], states near the Fermi level are still predominantly associated with edge and defect carbon atoms, with edge carbon atoms providing a major contribution. However, with the increase of W, the defect-influenced BMSs (EGNR-3-1, EGNR-3-3, and EGNR-3-5) have been transitioned to an edge-dominated regular magnetic semiconductor (EGNR-3-7), attributed to the reduction in quantum confinement effects and the diminishing influence of spin-polarized internal defect states.

Furthermore, we explored the influence of varying the distance (D) between the central defect areas and the edge regions on the electronic properties of EGNRs, using EGNR-3-1 as a reference model. This was achieved by integrating ZGNRs between these regions. The resultant structures, labeled EGNR-3-1-D1 and EGNR-3-1-D2, were differentiated based on the varying distances between the central defect areas and edge regions. Figure 7 illustrates these structures, along with their corresponding spin density distributions, band structures, and DOSs. Our results indicate that increasing D significantly affects the spin distributions and electronic properties. Specifically, as D grows, the spin distribution on defective carbon atoms decreases, aligning with our previous

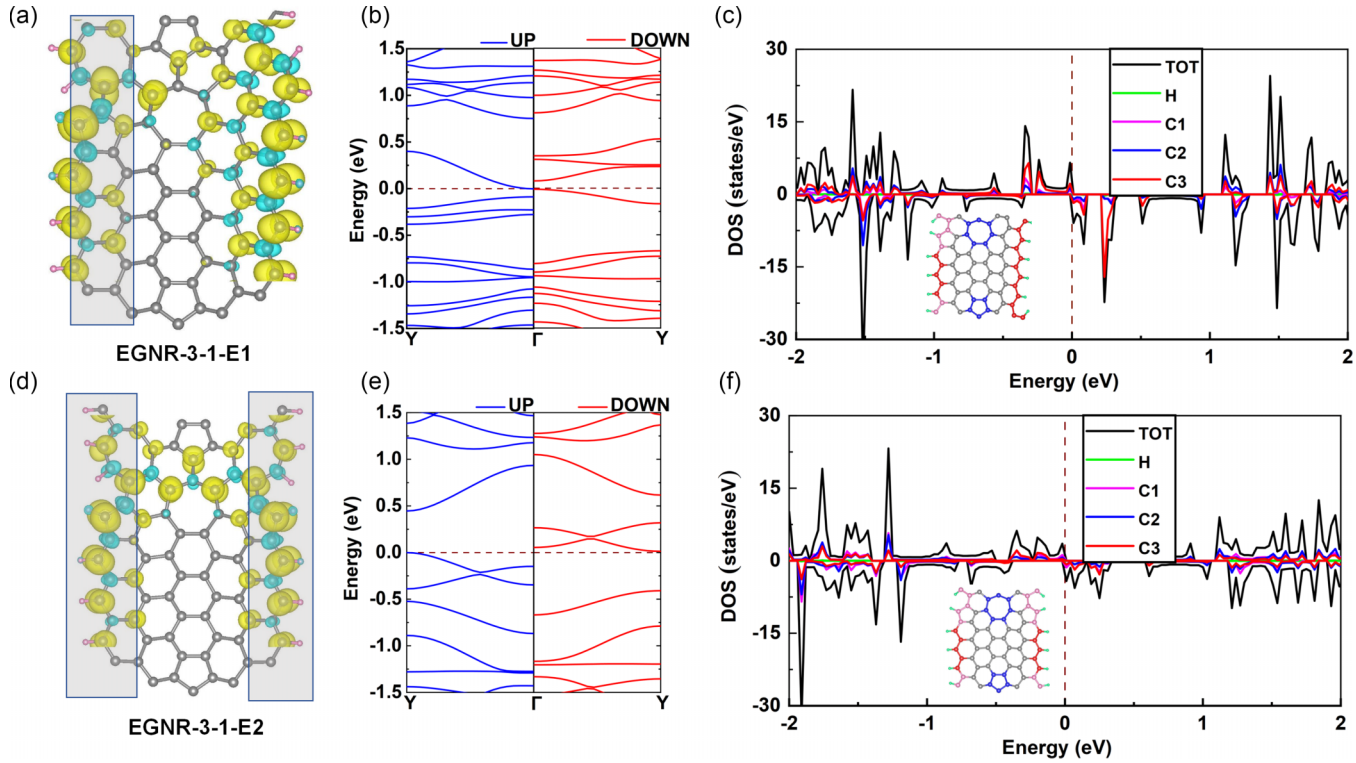

FIG. 8. Spin density distributions, band structures, and projected densities of states (PDOSs) for egg-tray graphene nanoribbons (EGNRs): (a)–(c) EGNR-3-1-E1 and (d)–(f) EGNR-3-1-E2. The value of the isosurface level is 0.002 e/Å^3. Black represents the total density of states (DOS); green, magenta, blue, and red represent the PDOSs of the hydrogen atoms (H), defective carbon atoms at the edge (C1), internal defect carbon atoms (C2), and edge carbon atoms (C3), respectively.

findings. In terms of band structures, as D increases, the CBM in the spin-up channel shifts lower, causing a reduction in the band gap for the spin-up channel from 0.73 to 0.14 eV. Concurrently, the VBM in the spin-down channel moves higher, resulting in a decrease in the band gap for the spin-down channel from 0.96 to 0.21 eV. Notably, in EGNR-3-1-D2, the CBM of the spin-up channel falls below the CBM of the spin-down channel, with both the CBM and VBM present in the spin-up channel, indicative of the properties of a magnetic semiconductor. Figures 7(c) and 7(f) visually demonstrate the evolution of electronic states near the Fermi level as D varies. In EGNR-3-1 [see Fig. 5(c)], the electronic states primarily originate from both the edge and internal defect carbon atoms. However, in EGNR-3-1-D1, while the states near the Fermi level still stem from both defect and edge carbon atoms, there is a noticeable change. The contribution from defect carbon atoms is significantly diminished, with most states now attributed to edge carbon atoms. Furthermore, in EGNR-3-1-D2, the contribution provided by defect carbon atoms near the Fermi level becomes almost undetectable. Therefore, when the distance between the central defect areas and the edge regions is sufficiently large, the electronic states of the edge regions predominantly determine the electronic properties of EGNR-3-1-D2, rendering it a magnetic semiconductor. These results reaffirm that the BMS properties of EGNRs arise from the unique synergistic interaction between the localized states associated with internal defects and their edge states. When the distance between these entities becomes excessively large, their interaction weakens, leading to the disappearance of BMS properties.

In these EGNRs, the edges are composed exclusively of hexagonal rings. Moving forward, we explore the impact of different topological structures of the edge carbon rings on the electronic properties of EGNRs by including pentagonal and heptagonal rings at the edges. Based on the structure of EGNR-3-1-D1, modifications were made to one or both edges, resulting in structures named EGNR-3-1-E1 (with one edge modified) and EGNR-3-1-E2 (with two edges modified), as depicted in Figs. 8(a) and 8(d), respectively. It is shown that, due to their narrower width, the spin density is distributed across both the edge carbon atoms and the central defect areas. The PDOS diagrams [see Figs. 8(c) and 8(f)] reveal that a significant portion of the states near the Fermi level originates from carbon atoms in the nonhexagonal rings of the edge structures. This results in a transformation of the electronic properties from BMS characteristic of EGNR-3-1-D1 to SGS observed in EGNR-3-1-E1 and EGNR-3-1-E2. The band structures of EGNR-3-1-E1 and EGNR-3-1-E2, presented in Figs. 8(b) and 8(d), respectively, show that the CBM and VBM reside in different spin channels and are both near the Fermi level, displaying SGS characteristics. These findings highlight the important role of edge structures in the emergence of BMS properties. Thus, the combined effects of internal defects, edge structures, and quantum confinement collectively contribute to the BMS properties in EGNRs.

IV. CONCLUSIONS

In this paper, we introduce an innovative approach to manipulate the spintronic properties of graphene nanoribbons, aiming to achieve BMSs through a synergistic effect induced by edges and internal defects. These graphene nanoribbons containing zigzag edges and internal defects are constructed by slicing ETG. These EGNRs exhibit remarkable stability, suggesting their high potential for successful experimental synthesis. Most EGNRs demonstrate FM ground states, with the narrowest EGNRs displaying either NM or AFM characteristics. The electronic and magnetic properties of EGNRs depend on the presence of internal defects, their dimensions, and the geometric configurations of the edges. Notably, when EGNRs possess moderate widths, the internal defect regions considerably affect the spin density distribution across the entire ribbon, resulting in spin polarization not only localized at the edge carbon atoms but also on the defective rings. This creates a synergistic effect that promotes the development of stable BMSs. An increase in the width of the EGNRs compresses the spin density distribution on the internal defects, gradually transforming the BMS to a conventional magnetic semiconductor or half-metal. Additionally, incorporating pentagons and heptagons at the edges of EGNRs converts the BMS into an SGS, thereby broadening their applicability in spintronics. In this paper, we broaden the spectrum of known BMSs and provide strategic insights for the development of future materials in spintronics.

ACKNOWLEDGMENTS

This paper is supported by the National Natural Science Foundation of China (Grants No. 11975206 and No. 12075211), the Natural Science Foundation of Zhejiang Province (Grant No. LQ20B030002), and the Scientific Research Foundation of Zhejiang A&F University (Grants No. 2019FR005 and No. 2019FR006). M.M. acknowledges the support of National Science Foundation (NSF) funds Grants No. DMR 1848141 and No. OAC 2117956, the Camille and Henry Dreyfus Foundation, and the CSU Research, Scholarly, and Creative Activity (RSCA) awards.

W.L., Y.C., and J.X. conceived the research; Y.C., J.X., and W.L. performed the calculations and analyzed the data; W.L., Y.C., and J.X. wrote the manuscript; M.M. helped to revise the manuscript. All authors discussed and commented on the manuscript.

The authors declare no competing financial or nonfinancial interests.

[1] X. Li and J. Yang, First-principles design of spintronics materials, Natl. Sci. Rev. **3**, 365 (2016).

[2] S. A. Wolf, D. D. Awschalom, R. A. Buhrman, J. M. Daughton, S. Von Molnár, M. L. Roukes, A. Y. Chtchelkanova, and D. M. Treger, Spintronics: A spin-based electronics vision for the future, Science **294**, 1488 (2001).

[3] X. Li and J. Yang, Bipolar magnetic materials for electrical manipulation of spin-polarization orientation, Phys. Chem. Chem. Phys. **15**, 15793 (2013).

[4] X. Li and J. Yang, Computational design of one-dimensional ferromagnetic semiconductors in transition metal embedded stannaspherene nanowires, Chin. J. Chem. **37**, 1021 (2019).

[5] J. Zhang, X. Li, and J. Yang, SiN-SiC nanofilm: A nanofunctional ceramic with bipolar magnetic semiconducting character, Appl. Phys. Lett. **104**, 172403 (2014).

[6] X. Li, X. Wu, Z. Li, J. Yang, and J. G. Hou, Bipolar magnetic semiconductors: A new class of spintronics materials, Nanoscale **4**, 5680 (2012).

[7] P. Gao, X. Li, and J. Yang, Proposed mechanical method for switching the spin transport channel in two-dimensional magnetic metal–magnetic semiconductor van der Waals contacts, Nanoscale Horiz. **5**, 1496 (2020).

[8] X. Li, X. Wu, and J. Yang, Control of spin in a La(Mn,Zn)AsO alloy by carrier doping, J. Mater. Chem. C **1**, 7197 (2013).

[9] F. Muñoz-Rojas, J. Fernandez-Rossier, and J. J. Palacios, Giant magnetoresistance in ultra-small graphene based devices, Phys. Rev. Lett. **102**, 136810 (2009).

[10] J. Zeng and K.-Q. Chen, Spin filtering, magnetic and electronic switching behaviors in manganese porphyrin-based spintronic devices, J. Mater. Chem. C **1**, 4014 (2013).

[11] M. Fischer, M. T. Elm, S. Sakita, S. Hara, and P. J. Klar, Magnetoresistance effects and spin-valve like behavior of an arrangement of two MnAs nanoclusters, Appl. Phys. Lett. **106**, 032401 (2015).

[12] M. G. Zeng, L. Shen, Y. Q. Cai, Z. D. Sha, and Y. P. Feng, Perfect spin-filter and spin-valve in carbon atomic chains, Appl. Phys. Lett. **96**, 042104 (2010).

[13] D. Zhang, M. Long, X. Zhang, F. Ouyang, M. Li, and H. Xu, Designing of spin-filtering devices in zigzag graphene nanoribbons heterojunctions by asymmetric hydrogenation and B-N doping, J. Appl. Phys. **117**, 014311 (2015).

[14] X. Q. Deng, Z. H. Zhang, G. P. Tang, Z. Q. Fan, and C. H. Yang, Spin filter effects in zigzag-edge graphene nanoribbons with symmetric and asymmetric edge hydrogenations, Carbon **66**, 646 (2014).

[15] J. Li, X. Li, and J. Yang, A review of bipolar magnetic semiconductors from theoretical aspects, Fundam. Res. **2**, 511 (2022).

[16] M. Zhang, X. Wang, H. Sun, N. Wang, J. He, N. Wang, Y. Long, C. Huang, and Y. Li, Induced ferromagnetic order of graphdiyne semiconductors by introducing a heteroatom, ACS Cent. Sci. **6**, 950 (2020).

[17] A. S. Mayorov, R. V. Gorbachev, S. V. Morozov, L. Britnell, R. Jalil, L. A. Ponomarenko, P. Blake, K. S. Novoselov, K. Watanabe, T. Taniguchi *et al.*, Micrometer-scale ballistic transport in encapsulated graphene at room temperature, Nano Lett. **11**, 2396 (2011).

[18] A. K. Y. Low, E. Vissol-Gaudin, Y.-F. Lim, and K. Hippalgaonkar, Mapping pareto fronts for efficient multi-objective materials discovery, J. Mater. Inform. **3**, 11 (2023).

[19] X. Song, K. Guo, H. Lu, D. Liu, and F. Tang, Modelling of phase stability: Integrating computational materials science and materials informatics, J. Mater. Inform. **1**, 7 (2021).

[20] W. Liu, J. Liu, J. Xia, H. Lin, and M. Miao, Bubble-wrap carbon: An integration of graphene and fullerenes, Nanoscale **10**, 11328 (2018).

[21] L. Zhao, W. Liu, W. Yi, T. Hu, D. Khodagholian, F. Gu, H. Lin, E. Zurek, Y. Zheng, and M. Miao, Nano-makisu: Highly anisotropic two-dimensional carbon allotropes made by weaving together nanotubes, Nanoscale **12**, 347 (2020).

[22] K. S. Novoselov, A. K. Geim, S. V. Morozov, D. Jiang, M. I. Katsnelson, I. V. Grigorieva, S. V. Dubonos, and A. A. Firsov, Two-dimensional gas of massless Dirac fermions in graphene, Nature (London) **438**, 197 (2005).

[23] S. V. Morozov, K. S. Novoselov, M. I. Katsnelson, F. Schedin, D. C. Elias, J. A. Jaszczak, and A. K. Geim, Giant intrinsic carrier mobilities in graphene and its bilayer, Phys. Rev. Lett. **100**, 016602 (2008).

[24] Y. Li, Z. Zhou, P. Shen, and Z. Chen, Electronic and magnetic properties of hybrid graphene nanoribbons with zigzag-armchair heterojunctions, J. Phys. Chem. C **116**, 208 (2012).

[25] W. Chen, Y. Sun, J. Guan, Q. Wang, X. Huang, and G. Yu, Molecular charge transfer via π-π interaction: An effective approach to realize the half-metallicity and spin-gapless-semiconductor in zigzag graphene nanoribbon, RSC Adv. **5**, 53003 (2015).

[26] L. Salemi, A. Lherbier, and J.-C. Charlier, Spin-dependent properties in zigzag graphene nanoribbons with phenyl-edge defects, Phys. Rev. B **98**, 214204 (2018).

[27] G. P. Tang, Z. H. Zhang, X. Q. Deng, Z. Q. Fan, and H. L. Zhu, Tuning spin polarization and spin transport of zigzag graphene nanoribbons by line defects, Phys. Chem. Chem. Phys. **17**, 638 (2015).

[28] Y.-W. Son, M. L. Cohen, and S. G. Louie, Half-metallic graphene nanoribbons, Nature (London) **444**, 347 (2006).

[29] E. Kan, Z. Li, J. Yang, and J. G. Hou, Half-metallicity in edge-modified zigzag graphene nanoribbons, J. Am. Chem. Soc. **130**, 4224 (2008).

[30] S. Mishra, D. Beyer, R. Berger, J. Liu, O. Gröning, J. I. Urgel, K. Müllen, P. Ruffieux, X. Feng, and R. Fasel, Topological defect-induced magnetism in a nanographene, J. Am. Chem. Soc. **142**, 1147 (2020).

[31] J. Bhattacharjee, Half-metallicity in graphene nanoribbons with topological defects at edge, J. Chem. Phys. **137**, 094705 (2012).

[32] W. Liu, L. Zhao, E. Zurek, J. Xia, Y. Zheng, H. Lin, J. Liu, and M. Miao, Building egg-tray-shaped graphenes that have superior mechanical strength and band gap, Npj Comput. Mater. **5**, 71 (2019).

[33] W. Kohn and L. J. Sham, Self-consistent equations including exchange and correlation effects, Phys. Rev. **140**, A1133 (1965).

[34] G. Kresse and J. Furthmüller, Efficient iterative schemes for *ab initio* total-energy calculations using a plane-wave basis set, Phys. Rev. B **54**, 11169 (1996).

[35] G. Kresse and D. Joubert, From ultrasoft pseudopotentials to the projector augmented-wave method, Phys. Rev. B **59**, 1758 (1999).

[36] J. P. Perdew, K. Burke, and M. Ernzerhof, Generalized gradient approximation made simple, Phys. Rev. Lett. **77**, 3865 (1996).

[37] J. Heyd, G. E. Scuseria, and M. Ernzerhof, Hybrid functionals based on a screened Coulomb potential, J. Chem. Phys. **118**, 8207 (2003).

[38] H. J. Monkhorst and J. D. Pack, Special points for Brillouin-zone integrations, Phys. Rev. B **13**, 5188 (1976).

[39] See Supplemental Material at http://link.aps.org/supplemental/10.1103/PhysRevB.110.085141 for the widths of EGNRs; magnetic moment M and magnetic susceptibility χ of EGNR-2-7; energy difference per unit cell of EGNR-2-1 as a function of carrier doping concentration; structures and band structures of EGNRs not shown in the main text; structures and band structures of the 2D configurations formed by EGNR-3-W and EGNR-4-W as W approaches infinity; and spin density distributions and band structure of 4-ZGNRs.

[40] Y.-X. Deng, S.-Z. Chen, Y. Zhang, X. Yu, Z.-X. Xie, L.-M. Tang, and K.-Q. Chen, Penta-hexa-graphene nanoribbons: Intrinsic magnetism and edge effect induce spin-gapless semiconducting and half-metallic properties, ACS Appl. Mater. Interfaces **12**, 53088 (2020).

[41] S. Nosé, A unified formulation of the constant temperature molecular dynamics methods, J. Chem. Phys. **81**, 511 (1984).

[42] G. Bussi, D. Donadio, and M. Parrinello, Canonical sampling through velocity rescaling, J. Chem. Phys. **126**, 014101 (2007).

[43] P. Ruffieux, S. Wang, B. Yang, C. S. Sánchez, J. Liu, T. Dienel, L. Talirz, P. Shinde, C. Pignedoli, D. Passerone *et al.*, On-surface synthesis of graphene nanoribbons with zigzag edge topology, Nature (London) **531**, 489 (2016).

[44] X. Dong, L. Wang, K. Li, H. Zheng, Y. Wang, Y. Meng, H. Shu, H. Mao, S. Feng, and C. Jin, Tailored synthesis of the narrowest zigzag graphene nanoribbon structure by compressing the lithium acetylide under high temperature, J. Phys. Chem. C **122**, 20506 (2018).

[45] K. Y. Cheung, X. Xu, and Q. Miao, Aromatic saddles containing two heptagons, J. Am. Chem. Soc. **137**, 3910 (2015).

[46] H. Prinzbach, A. Weiler, P. Landenberger, F. Wahl, J. Wörth, L. T. Scott, M. Gelmont, D. Olevano, and B. V. Issendorff, Gas-phase production and photoelectron spectroscopy of the smallest fullerene, C20, Nature (London) **407**, 60 (2000).

[47] J. Li, X. Li, J. Feng, W. Yao, H. Zhang, C. Lu, and R. Liu, Organocatalytic enantioselective synthesis of seven-membered ring with inherent chirality, Angew. Chem. Int. Ed. **63**, e202319289 (2024).

[48] R. S. Doerksen, T. Hodík, G. Hu, N. O. Huynh, W. G. Shuler, and M. J. Krische, Ruthenium-catalyzed cycloadditions to form five-, six-, and seven-membered rings, Chem. Rev. **121**, 4045 (2021).

[49] Y. Fei and J. Liu, Synthesis of defective nanographenes containing joined pentagons and heptagons, Adv. Sci. **9**, 2201000 (2022).

[50] L.-P. Tang, Q.-Z. Li, C.-X. Zhang, F. Ning, W.-X. Zhou, L.-M. Tang, and K.-Q. Chen, Prediction of intrinsic ferromagnetism in two-dimension planar metal-organic framework semiconductors, J. Magn. Magn. Mater. **488**, 165354 (2019).

[51] Y. Zhang, B. Wang, Y. Guo, Q. Li, and J. Wang, A universal framework for Metropolis Monte Carlo simulation of magnetic curie temperature, Comput. Mater. Sci. **197**, 110638 (2021).

[52] J. Kunstmann, C. Özdoğan, A. Quandt, and H. Fehske, Stability of edge states and edge magnetism in graphene nanoribbons, Phys. Rev. B **83**, 045414 (2011).

[53] O. V. Yazyev and M. I. Katsnelson, Magnetic correlations at graphene edges: Basis for novel spintronics devices, Phys. Rev. Lett. **100**, 047209 (2008).

[54] L. B. Drissi, S. Zriouel, and E. H. Saidi, Edge effect on magnetic phases of doped zigzag graphone nanoribbons, J. Magn. Magn. Mater. **374**, 394 (2015).

[55] F. Wu, E. Kan, H. Xiang, S.-H. Wei, M.-H. Whangbo, and J. Yang, Magnetic states of zigzag graphene nanoribbons from first principles, Appl. Phys. Lett. **94**, 223105 (2009).

[56] S. Bhowmick, A. Medhi, and V. B. Shenoy, Sensory-organ-like response determines the magnetism of zigzag-edged honeycomb nanoribbons, Phys. Rev. B **87**, 085412 (2013).

[57] C. Guo, Z. H. Zhang, G. Kwong, J. B. Pan, X. Q. Deng, and J. J. Zhang, Enormously enhanced rectifying performances by modification of carbon chains for D-σ-A molecular devices, J. Phys. Chem. C **116**, 12900 (2012).

[58] M. Slota, A. Keerthi, W. K. Myers, E. Tretyakov, M. Baumgarten, A. Ardavan, H. Sadeghi, C. J. Lambert, A. Narita, K. Müllen, and L. Bogani, Magnetic edge states and coherent manipulation of graphene nanoribbons, Nature **557**, 691 (2018).

[59] X. Xu, K. Sun, A. Ishikawa, A. Narita, and S. Kawai, Magnetism in nonplanar zigzag edge termini of graphene nanoribbons, Angew. Chem. Int. Ed. **62**, e202302534 (2023).